# Implication of Mismatch Between Stress and Strain-Rate in Turbulence Subjected to Rapid Straining and Destraining on Dynamic LES Models

**Jun Chen**
Department of Mechanical Engineering, Johns Hopkins University, 223 Latrobe Hall, 3400 North Charles Street, Baltimore, MD 21218
e-mail: junchen@jhu.edu
Phone: 1-410-516-5427

**Joseph Katz**
Department of Mechanical Engineering, Johns Hopkins University, 118 Latrobe Hall, 3400 North Charles Street, Baltimore, MD 21218
e-mail: katz@jhu.edu
Phone: 1-410-516-5470

**Charles Meneveau**
Department of Mechanical Engineering, Johns Hopkins University, 127 Latrobe Hall, 3400 North Charles Street, Baltimore, MD 21218
e-mail: meneveau@jhu.edu
Phone: 1-410-516-7802

*Planar straining and destraining of turbulence is an idealized form of turbulence-meanflow interaction that is representative of many complex engineering applications. This paper studies experimentally the response of turbulence subjected to a process involving planar straining, a brief relaxation and destraining. Subsequent analysis quantifies the impact of the applied distortions on model coefficients of various eddy viscosity subgrid-scale models. The data are obtained using planar particle image velocimetry (PIV) in a water tank, in which high Reynolds number turbulence with very low mean velocity is generated by an array of spinning grids. Planar straining and destraining mean flows are produced by pushing and pulling a rectangular piston towards and away from the bottom wall of the tank. The velocity distributions are processed to yield the time evolution of mean subgrid dissipation rate, the Smagorinsky and dynamic model coefficients, as well as the mean subgrid-scale momentum flux during the entire process. It is found that the Smagorinsky coefficient is strongly scale dependent during periods of straining and destraining. The standard dynamic approach overpredicts the dissipation based Smagorinsky coefficient, with the model coefficient at scale $\Delta$ in the standard dynamic Smagorinsky model being close to the dissipation based Smagorinsky coefficient at scale $2\Delta$. The scale-dependent Smagorinsky model, which is designed to compensate for such discrepancies, yields unsatisfactory results due to subtle phase lags between the responses of the subgrid-scale stress and strain-rate tensors to the applied strains. Time lags are also observed for the SGS momentum flux at the larger filter scales considered. The dynamic and scale-dependent dynamic nonlinear mixed models do not show a significant improvement. These potential problems of SGS models suggest that more research is needed to further improve and validate SGS models in highly unsteady flows.* [DOI: 10.1115/1.1989360]

## 1 Introduction

In most engineering applications, turbulent flows are regularly subjected to strong large-scale mean deformation. Examples include turbulent flows inside contracting or expanding channels, flows inside pumps, flows around propellers, etc. When the turbulence-to-mean-shear time scale ratio is large enough, namely $S\cdot k/\varepsilon\rightarrow\infty$ ($S$ is the mean strain; $k\equiv 0.5\langle u_i' u_i'\rangle$ is the turbulence kinetic energy with $\langle\cdot\rangle$ denoting the averaging operation; and $\varepsilon$ is the dissipation rate), the evolution of turbulence can be predicted by rapid-distortion theory (RDT), which neglects the nonlinear terms in the evolution equation of turbulence, thus the equation can be solved analytically (e.g., Ref. [1]). However, in many engineering flows, the turbulence-to-mean-shear time scale ratio is large, but not large enough to apply RDT.

The interactions between turbulence and strong mean straining flow have already been studied extensively. Townsend [2], Keffer [3], and Tucker and Reynolds [4] conducted hot-wire measurements of decaying grid turbulence inside a specially designed, distorting section of wind tunnel. Lee and Reynolds [5] performed direct numerical simulations (DNS) of turbulence response to several types of irrotational straining, including planar and axisymmetric straining. The simulations were performed at a Taylor microscale Reynolds number, $\mathrm{Re}_\lambda = u\lambda/\nu$, of less than 100, where $u$ is the characteristic turbulent fluctuation and $\lambda$ is the Taylor microscale.

Presently, large eddy simulation (LES) is the most rapidly developing turbulence prediction technique. Thus, it is of considerable interest to study the effects of straining on turbulence from the point of view of LES. Liu et al. [6] studied scale interactions and evolution of statistics of subgrid-scale (SGS) variables of interest in LES during axisymmetric distortion with $S\cdot k/\varepsilon\sim 7$ and $\mathrm{Re}_\lambda\sim 290$. They concluded that the simple Smagorinsky eddy-viscosity SGS model overpredicts the SGS dissipation, i.e., the flow of energy to scales smaller than the filter scale, during strong straining, and that mixed model formulations improve the model performance. The moderate Reynolds number and limited data of the Liu et al. study prevented detailed tests of the popular dynamic model [7]. Due to limitations of their experimental setup, Liu et al. only studied the effect of axisymmetric straining, and there was no possibility to study return-to-isotropy, relaxation, or destraining.

In the present study we experimentally investigate the evolution of flow variables in a cycle consisting of planar straining, relaxation, and destraining. Such a scenario is a simplification of many engineering flows, e.g., turbulence passing around a propeller blade. There, the turbulence is strained near the leading edge of the blade, and the deformation is partially reversed during the

Contributed by the Fluids Engineering Division for publication in the JOURNAL OF FLUIDS ENGINEERING. Manuscript received by the Fluids Engineering Division, August 5, 2004; Final revision: June 1, 2005. Associate Editor: Ismail Celik.

  

pressure recovery region, towards the trailing edge of the blade. If the flow is not massively separated, and the blade is long (almost 2D), 2-D irrotational straining (stagnation point flow) is a reasonable idealization. The main focus of this study is the response of the Smagorinsky model at various filter scales, and the performance of the dynamic and scale-dependent dynamic Smagorinsky models in reproducing the measured evolution of the Smagorinsky coefficient. A brief review of LES modeling issues, including the Smagorinsky and nonlinear mixed SGS models, is given in Sec. 2. Also discussed are the standard dynamic and scale-dependent dynamic approaches to determine the model coefficients. Details about the experimental facility and instrumentation are presented in Sec. 3. The characteristics of mean flow and turbulence before straining are documented in Sec. 4. The evolution of SGS dissipation, and a priori tests of the Smagorinksy and nonlinear mixed models are shown in Sec. 5. The performance of the Smagorinsky model for prediction of SGS momentum flux is quantified in Sec. 6. Conclusions are presented in Sec. 7.

## 2 Large Eddy Simulation and SGS Stress Models

Proposed in the 1960s, large eddy simulation provides a promising approach to numerically study engineering flows with complex geometry at high Reynolds number [8,9]. LES decomposes the flow variables into resolved and unresolved (subgrid scale) parts by applying a filtering operation given by

$$\widetilde{f}(\mathbf{x},t)=\int_D f(\mathbf{x}',t)G_\Delta(\mathbf{x},\mathbf{x}')d\mathbf{x}', \tag{1}$$

where $D$ is the computational domain and $G_\Delta$ is a filtering kernel with a characteristic scale $\Delta$. For incompressible flows, the filtered Navier-Stokes equations solved in LES are

$$\begin{aligned}\frac{\partial \widetilde{u}_i}{\partial x_i}&=0,\\ \frac{\partial \widetilde{u}_i}{\partial t}+\widetilde{u}_j\frac{\partial \widetilde{u}_i}{\partial x_j}&=-\frac{\partial}{\partial x_j}\left[\frac{\widetilde{p}}{\rho}\delta_{ij}+\tau_{ij}\right]+\nu\frac{\partial^2\widetilde{u}_i}{\partial x_j^2},\end{aligned} \tag{2}$$

where the subgrid-scale (SGS) stress, $\tau_{ij}$, is defined as

$$\tau_{ij}=\widetilde{u_iu_j}-\widetilde{u}_i\widetilde{u}_j. \tag{3}$$

The SGS stress must be modeled properly in order to close the equation system (2).

Scale interactions, such as energy transfer between resolved and SGS scales, referring to scales larger and smaller than $\Delta$, respectively, are fundamental physical phenomena in turbulent flows. Understanding the processes underlying the energy transfer in a turbulent field is important in successful application of LES. The influence of the SGS stresses on the resolved flow field is reflected in the transport equation of resolved and/or subgrid kinetic energy [10]. The so-called sub-grid scale energy dissipation,

$$\Pi_\Delta=-\langle\tau_{ij}\widetilde{S}_{ij}\rangle, \tag{4}$$

where

$$\widetilde{S}_{ij}=\frac{1}{2}\left(\frac{\partial\widetilde{u}_i}{\partial x_j}+\frac{\partial\widetilde{u}_j}{\partial x_i}\right) \tag{5}$$

is the resolved strain-rate tensor, plays a vital role in these equations. The SGS dissipation enters as a sink in the transport equation for mean resolved kinetic energy, and as a source term in the equation for unresolved kinetic energy [10]. It thus quantitatively describes the net energy transfer between resolved and subgrid scales. While the overall trend of energy transfer is typically from resolved to subgrid scales (forward scattering), there are locations in the flow field where the subgrid scales return energy to resolved scales (back scattering) [10,11]. In the inertial range, the mean SGS dissipation is dominant in the energy budget. Thus, its key features must be reproduced properly by SGS models.

Many different SGS models have been proposed (see reviews in Refs. [8,12]). The most popular are of the eddy-viscosity type

$$\tau_{ij}^{Smag}=-2\nu_T\widetilde{S}_{ij}, \tag{6}$$

where $\nu_T$ is the scalar eddy viscosity which relates the deviatoric part of the SGS stress to the resolved strain. The Smagorinsky model [13] is a representative of this class with

$$\nu_T=(C_S^\Delta\Delta)^2|\widetilde{S}|, \tag{7}$$

where $C_S^\Delta$ is the (Static) Smagorinsky coefficient and $|\widetilde{S}|=\sqrt{2\widetilde{S}_{ij}\widetilde{S}_{ij}}$. The so-called nonlinear mixed SGS model was proposed by applying a Taylor series expansion of $\widetilde{u}_i$ and adding the Smagorinsky model as a dissipative term [14–16]:

$$\tau_{ij}^{NL}=-2(C_{S,NL}^\Delta\Delta)^2|\widetilde{S}|\widetilde{S}_{ij}+\frac{1}{12}\Delta^2\frac{\partial\widetilde{u}_i}{\partial x_l}\frac{\partial\widetilde{u}_j}{\partial x_l} \tag{8}$$

with a model coefficient $C_{S,NL}^\Delta$ (the subscript "*NL*" denotes the nonlinear mixed model). Other widely used models are reviewed in Ref. [15].

The performance of SGS models can be evaluated by a priori tests, and by a posteriori tests [17]. In a priori tests, some selected features of the modeled stresses, $\tau_{ij}^{\mathrm{mod}}(\mathbf{x},t)$, are compared with the "real" SGS stresses, $\tau_{ij}(\mathbf{x},t)$, calculated using its definition, i.e., Eq. (3). Since a necessary condition for LES to be considered successful is that it yield correct energetics of the resolved flow, SGS models can be tested a priori by comparing the relevant effect of the SGS stresses upon the energetics, namely by comparing the measured mean SGS dissipation with the modeled mean SGS dissipation, $-\langle\tau_{ij}^{\mathrm{mod}}\widetilde{S}_{ij}\rangle$ [18].

Experiments have provided data for a priori tests of SGS models, typically in flow fields whose Reynolds numbers are higher than those provided by DNS. For example, Liu et al. [11] applied particle image velocimetry (PIV) in a turbulent jet at $\mathrm{Re}_\lambda\approx310$, and studied the performance of several SGS models. O'Neil and Meneveau [19] conducted hot-wire measurements in a turbulent plane wake at $\mathrm{Re}_\lambda\approx500$. Tao et al. [20] evaluated the statistical geometry of subgrid-scale stresses based on 3-D holographic PIV measurement in a duct flow at $\mathrm{Re}_\lambda\approx260$. Porte-Agel et al. [21] and Kleissl et al. [22] performed a priori tests using field experimental data of atmospheric boundary layer, collected by arrays of sonic anemometers. These investigations have provided considerable insight into the underlying physics of SGS dynamics, and quantified the effects of various flow parameters, such as stratification [22].

The static Smagorinsky model [13] is expressed by employing a scale-invariant constant for $C_S$, and its value is $C_S\approx0.16$ [23]. It is well known that a constant scale-invariant coefficient is not appropriate in complex engineering flows (e.g., Ref. [15]). Germano et al. [7,24] proposed a dynamic Smagorinsky model to determine the model coefficient locally from the resolved scales. A test filter at scale $\alpha\Delta$ (typically $\alpha=2$) is adopted and the model coefficient is determined using [24]

$$(C_S^{\Delta,DM})^2=\frac{\langle L_{ij}M_{ij}\rangle}{\langle M_{ij}M_{ij}\rangle}, \tag{9}$$

where $L_{ij}=\overline{\widetilde{u}_i\widetilde{u}_j}-\overline{\widetilde{u}}_i\cdot\overline{\widetilde{u}}_j$ and $M_{ij}=-2\Delta^2(\alpha^2|\overline{\widetilde{S}}|\overline{\widetilde{S}}_{ij}-\overline{|\widetilde{S}|\widetilde{S}_{ij}})$, and $\bar{(\ )}$ indicates filtering at $\alpha\Delta$. The averaging is done over spatial domains of statistical homogeneity or by following a fluid element in time, as in the Lagrangian dynamic model [25]. A central assumption of the traditional dynamic model is scale invariance, i.e., $C_S^\Delta=C_S^{\alpha\Delta}$ [15]. For complex flows, where this assumption is not valid (as will be seen to occur during straining of turbulence in the present analysis), a new scale-dependent dynamic model was proposed by Porte-Agel et al. [26]. In this approach, the ratio of the coefficient at two scales

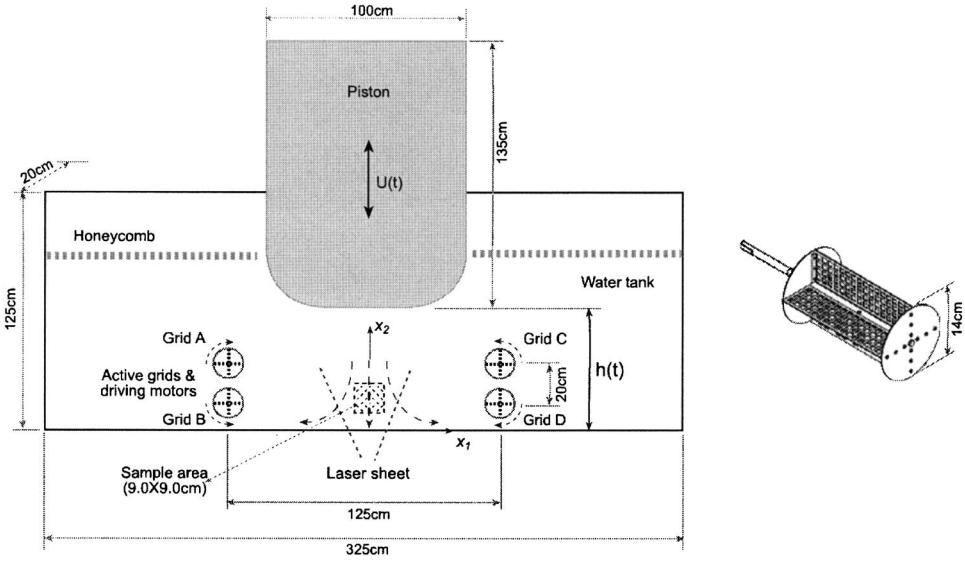


**Fig. 1 Schematic description of (*a*) the experimental facility and (*b*) the activity grid**

$$\beta = \frac{(C_S^{\alpha\Delta,DM})^2}{(C_S^{\Delta,DM})^2} \tag{10}$$

is introduced as another variable (a scale-dependence correction factor), to be determined dynamically. Implementation of this model involves a second test-filtering at a larger scale, $\alpha^2\Delta$, and an assumption that the scale-dependence correction factor is in itself scale-invariant, i.e.,

$$\beta = \frac{(C_S^{\alpha\Delta,DM})^2}{(C_S^{\Delta,DM})^2} = \frac{(C_S^{\alpha^2\Delta,DM})^2}{(C_S^{\alpha\Delta,DM})^2}. \tag{11}$$

As shown in Porte-Agel et al. [26], substituting in a pair of Germano identities [7] at both test-filter scales provides a solution for $\beta$ from a polynomial equation, which is constructed from the first test filtering at a scale $\alpha\Delta$, and the second test filtering at scale $\alpha^2\Delta$ (denoted by $\hat{(\,)}$). Then, the tensor $M_{ij} = -2\Delta^2(\beta\alpha^2|\bar{\tilde{S}}|\bar{\tilde{S}}_{ij} - \widehat{|\tilde{S}|\tilde{S}_{ij}})$ is evaluated with the actual value of $\beta$. Solution of the polynomial equation can be quite cumbersome, especially in conjunction with the Lagrangian dynamic model. To simplify the formulation, Bou-Zeid et al. [27] proposed to utilize the observation [28,26] that the standard dynamic model yields the model coefficient appropriate to the test-filter scale, and not to that of the basic grid filter scale, i.e.,

$$(C_S^{\alpha\Delta})^2 \approx (C_S^{\Delta,DM})^2 = \frac{\langle L_{ij}M_{ij}\rangle}{\langle M_{ij}M_{ij}\rangle}, \tag{12}$$

where $M_{ij}$ is evaluated assuming that $\beta = 1$. This observation was made in the scale-dependent cases, when the filter scale tends to the Kolmogorov scale [28], or to the integral scale near a solid wall [28]. One of the objectives of the present work is to test whether this observation holds also in the case of strained turbulence. Since in LES we require the coefficient at scale $\Delta$ and not at $\alpha\Delta$, by using a second test-filter, we can write

$$(C_S^{\alpha^2\Delta})^2 \approx (C_S^{\alpha\Delta,DM})^2 = \frac{\langle Q_{ij}N_{ij}\rangle}{\langle N_{ij}N_{ij}\rangle}, \tag{13}$$

where $Q_{ij} = \widehat{\tilde{u}_i\tilde{u}_j} - \hat{\tilde{u}}_i\hat{\tilde{u}}_j$ and $N_{ij} = -2\Delta^2(\alpha^2|\hat{\tilde{S}}|\hat{\tilde{S}}_{ij} - \widehat{|\tilde{S}|\tilde{S}_{ij}})$. Then, $\beta$ is computed as the ratio of Eqs. (12) and (13), and assuming that $\beta$ is scale invariant, the scale-dependent dynamic model coefficient at scale $\Delta$ ($C_S^{\Delta,SDDM}$) can be expressed as a geometric extrapolation

$$(C_S^{\Delta,SDDM})^2 = \frac{(C_S^{\Delta,DM})^4}{(C_S^{\alpha\Delta,DM})^2}. \tag{14}$$

The aforementioned dynamic approaches can also be used to determine the eddy-viscosity coefficient in the nonlinear mixed model, Eq. (8), and one obtains

$$(C_{S,NL}^{\Delta,DM})^2 = \frac{\langle L_{ij}M_{ij}\rangle - \langle Y_{ij}M_{ij}\rangle}{\langle M_{ij}M_{ij}\rangle}, \tag{15}$$

where

$$Y_{ij} = \frac{1}{12}\Delta^2\left(\alpha^2\frac{\partial\bar{\tilde{u}}_i}{\partial x_l}\frac{\partial\bar{\tilde{u}}_j}{\partial x_l} - \overline{\frac{\partial\tilde{u}_i}{\partial x_l}\frac{\partial\tilde{u}_j}{\partial x_l}}\right).$$

Moreover, if the scale-dependent dynamic approach is applied, the nonlinear mixed model coefficient can be determined by

$$(C_{S,NL}^{\Delta,SDDM})^2 = \frac{(C_{S,NL}^{\Delta,DM})^4}{(C_{S,NL}^{\alpha\Delta,DM})^2} \tag{16}$$

with

$$(C_{S,NL}^{\alpha\Delta,DM})^2 = \frac{\langle Q_{ij}N_{ij}\rangle - \langle Z_{ij}N_{ij}\rangle}{\langle N_{ij}N_{ij}\rangle},$$

where

$$Z_{ij} = \frac{1}{12}\Delta^2\left(\alpha^2\frac{\partial\hat{\tilde{u}}_i}{\partial x_l}\frac{\partial\hat{\tilde{u}}_j}{\partial x_l} - \widehat{\frac{\partial\tilde{u}_i}{\partial x_l}\frac{\partial\tilde{u}_j}{\partial x_l}}\right).$$

Later in this paper we use PIV data to evaluate the evolution of measured and modeled SGS dissipation at various scales, and the resulting impact on the modeled coefficients introduced in this section.

## 3 Experimental Setup

**3.1 Facility.** A schematic description of the test facility is shown in Fig. 1. The experimental setup is composed of two subsystems. The first one generates homogeneous, isotropic turbulence (initial equilibrium turbulence) at moderately high Reynolds numbers. The turbulence is generated using symmetrically located four active grids driven by four synchronized motors whose operating parameters are adjusted to obtain near zero mean velocity prior to straining. The second subsystem applies uniform straining-relaxation-destraining on the turbulence by translating a piston vertically at prescribed velocities. The piston occupies almost the entire width of the tank. The dimensions of the water tank are 325 cm (L) $\times$ 125 cm (H) $\times$ 20 cm (W). The sample area ($10 \times 10$ cm$^2$) is located near the center-bottom of the tank, as indicated by dashed lines in Fig. 1. Windows below and on both sides of the sample area provide optical access for PIV measurement.

Active grids have been proven to be an effective method to generate high Reynolds number isotropic turbulence. For example, Makita [29] utilized an agitator wing array driven by stepping motors in a wind tunnel. Mydlarski and Warhaft [30] employed the same idea to study the characteristics of turbulence with $\mathrm{Re}_\lambda$ varying from 50 to 473. Liu et al. [6] introduced the four rotating grids inside a small water tank to generate high-intensity turbulence with very little mean flow. The present rotating grid is shown in Fig. 1(*b*). It has four blades made of perforated metal plates with a solidity of 40%. Each grid is independently driven by a $\frac{1}{2}$ horsepower ac motor, with variable frequency inverter providing speed control. The grids can be maintained at a stable speed up to 500 rpm. The speed of each grid is adjusted separately to optimize the homogeneity of turbulence in the test section, as determined from repeated measurements. For all the data discussed in this paper, the bottom two grids are operated at a constant speed of 450 rpm and the top two at 375 rpm. The differences in speed are needed to achieve acceptable spatial uniformity of the turbulence.

When the piston moves vertically, the flow pattern under it becomes a 2-D stagnation-point flow with spatially uniform strain rate. The resulting strain rate tensor is

$$\mathbf{S}(t) = S(t)\begin{bmatrix} 1 & 0 & 0 \\ 0 & -1 & 0 \\ 0 & 0 & 0 \end{bmatrix}, \tag{17}$$

where $S(t)$ is the strain rate magnitude. Moreover, if the piston elevation, $h(t)$, is exponential in time, i.e.,

$$h(t) = He^{-S(t-t_0)} \tag{18}$$

the strain rate is also time independent.

The bottom surface of the piston has rounded corners to prevent possible flow separation which is critical when the flow is destrained. The piston is driven by a motion control system through a lever with a magnification ratio of 3. The motion control system consists of an Exlar GS60-1010 linear electric actuator, an Emerson MX-1600 brushless drive, and an Emerson AXIMA 2000 programmable motion control module, as illustrated in Fig. 2. The dynamic load rating of the actuator is 21,200 N, and its maximum velocity is 1.018 m/s. The stroke of the actuator is 25.4 cm, i.e., the maximum displacement of the piston is 76.2 cm. The trajectory of the piston is programmed through the motion control module, enabling us to adjust the relevant parameters and to obtain different trajectories. Two honeycombs (8.0 cm thick, 1.0 cm cell diameter) are placed near the top part of the water tank to alleviate the influence of surface waves.

The trajectory of the piston designed for this study is shown in Fig. 3. In each cycle, the piston moves downward to generate straining, rests for some time (relaxation), and then moves upward to generate destraining. Details of the actual piston's trajectory and its effect on the flow will be analyzed in the next section. The trajectory of the piston is monitored by a high-speed video camera (Kodak Ektapro EM) operating at 250 frames per second, as shown in Fig. 2. Results confirm that the motion control system is repeatable. The rms value of variance between piston trajectories in different runs at any given time is about 2 mm.

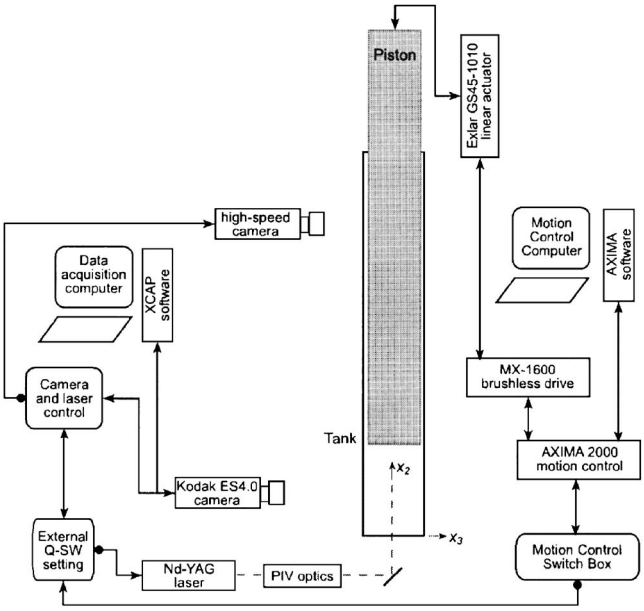


**Fig. 2 Schematics of the instrumentation and control system**

**3.2 Instrumentation.** Particle image velocimetry (PIV) is used to measure the velocity field. The flow field is seeded with hollow glass beads (median diameter 10 $\mu$m, specific gravity 1.1). The light source is a dual-head Nd-YAG laser (532 nm, 120 mJ) whose beam is expanded to a sheet and illuminates the $x_1$-$x_2$ plane along the centerline of the tank. A Kodak ES-4.0 digital camera, with 2048 pixel $\times$ 2048 pixel resolution, operating at 5 Hz under double-exposure mode, is used to record images. The sample area is $9.0 \times 9.0$ cm$^2$ of which the upper $9.0 \times 7.5$ cm$^2$ is used during the analysis. The lower 1.5 cm part shows some bottom effects and thus is discarded. The analysis consists of image enhancement, followed by cross correlation to determine the velocity [31,32]. The size of interrogation windows is $32 \times 32$ pixel. With 50% overlap, the vector spacing is 0.7 mm. A total of $120 \times 100$ vectors are obtained from each image pair.

As shown in Fig. 2, the motion control system and the PIV measurement are synchronized in order to obtain repeated mea-

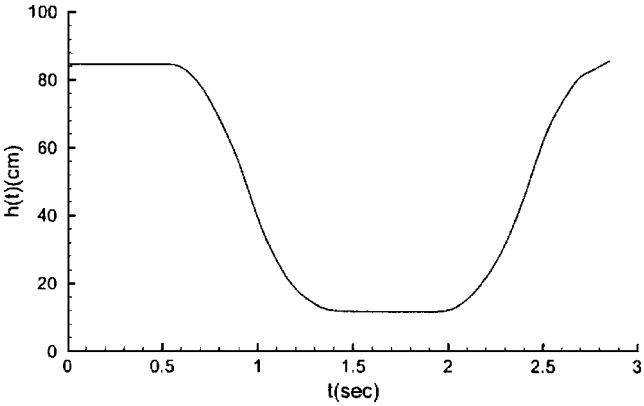


**Fig. 3 Piston motion trajectory**

surements at exactly the same time in every cycle. Repeated measurements enable us to calculate the ensemble statistics as a function of phase in the piston cycle. Since the present camera operates up to 5 Hz under the double-exposure mode, the temporal resolution of the measurements is 0.2 s. To increase the temporal resolution of the statistics, we record sequences at varying initial delay. The data are obtained at a total of 48 phases during the trajectory cycle providing a temporal resolution of 0.05 s. Since no frequency spectra or time derivative are needed, this resolution is appropriate for this study. At every time step, the measurement is repeated 1000 times, which provides a good ensemble set for statistical analysis and statistical convergence. The minimum interval between adjacent repeated measurements is set to 3 min, so that the background turbulence in later runs is not influenced by the history of previous runs.

The typical conservative uncertainty of the instantaneous data is 0.2 pixels, and the relative uncertainty is about 2% (for a characteristic displacement of 10.0 pixels). Consequently, the uncertainty in the mean velocity (ensemble set of 1000) is 0.06%, and the rms value is 0.4%. The uncertainty in terms involving mean velocity gradient is about 0.5%. Further details on errors and uncertainties in the present analysis procedure are presented in Roth et al. [31] and Roth and Katz [32]. Extended discussion on uncertainties in PIV data analysis can be found in Refs. [33–35], etc.

## 4 Flow Characterization

**4.1 Mean Flow.** Prior to straining, the flow consists of the grid generated turbulence, whereas during the straining one can identify the stagnation point flow along with the turbulence. The characteristics of the mean flow are evaluated by calculating an ensemble mean of velocity components, $U_1(\mathbf{x},t)$ and $U_2(\mathbf{x},t)$, at every point. Figure 4 shows some streamlines of the mean flow at $t=1.160$ s and $t=2.160$ s, corresponding to the times with strong straining and destraining, respectively. The mean flow is of stagnation-point-type in both cases.

The strain rate of mean flow is then evaluated from the data using central finite differencing:

$$\begin{cases} S_{11}(\mathbf{x},t) = \partial U_1(\mathbf{x},t)/\partial x_1, \\ S_{22}(\mathbf{x},t) = \partial U_2(\mathbf{x},t)/\partial x_2, \end{cases} \qquad S = (S_{11} - S_{22})/2. \tag{19}$$

The evolution of the spatially averaged strain rate of mean flow is presented in Fig. 5. The error bars represent the standard deviation of the local values from the spatially averaged strain, i.e., the applied straining and destraining are nearly uniform across the field of view. According to the sign of mean straining, the cycle can be divided into four regimes: initial equilibrium, plane straining, relaxation, and plane destraining. The magnitudes of peak straining and destraining are both about 3.5 $s^{-1}$.

**4.2 Initial Equilibrium Turbulence.** The fluctuating velocity components are calculated from the measured velocity, $u_i(\mathbf{x},t)$, using Reynolds decomposition:

$$u_i'(\mathbf{x},t) \equiv u_i(\mathbf{x},t) - U_i(\mathbf{x},t). \tag{20}$$

The mean and rms values of the initial equilibrium turbulence, $U_i$ and $u_i^{rms}=\langle u_i' u_i' \rangle^{1/2}$ (no summation over $i$), are analyzed based on the data ensemble at $t=0.210$ s. The mean values of the two velocity components, $U_1 \approx 0.003$ m/s and $U_2 \approx 0.029$ m/s, are much weaker than the mean velocity applied by straining and destraining. The initial spatial mean of the rms velocity fluctuations are $u_1^{rms} \approx 0.084$ m/s and $u_2^{rms} \approx 0.076$ m/s. Their spatial distributions, shown in Fig. 6, display good spatial homogeneity for both components. The homogeneity at different scales is also verified by comparing energy spectra at different locations in the field (not shown). Figure 7 shows the one-dimensional kinetic energy spectra of the initial equilibrium turbulence. The spectra are calculated using data along four lines near the image center, horizontal lines for $\kappa_1$ and vertical lines for $\kappa_2$. The ensemble mean velocity of every point is subtracted, and the data are linearly detrended, i.e., the mean linear trend of the finite instantaneous data (determined through least-square fit) is subtracted from the original values. This procedure maintains only the fluctuating components with nearly periodic boundary conditions for spectral analysis. There is no additional windowing assuring minimal impact on the variance, as discussed in Ref. [36]. The spectra are calculated using fast Fourier transforms (FFTs), and then averaged over the four lines, and over the 1000 realizations in the ensemble set. Two longitudinal, $E_{11}(\kappa_1)$ and $E_{22}(\kappa_2)$, and two transverse, $\frac{3}{4}E_{11}(\kappa_2)$ and $\frac{3}{4}E_{22}(\kappa_1)$, spectra in both directions, are presented. The four curves show fairly good agreement except at the high wave number range, which verifies that the initial equilibrium turbulence is nearly isotropic [37]. In the inertial range of homogeneous isotropic turbulence

$$E_{11}(\kappa_1) = \tfrac{18}{55} C_\kappa \varepsilon^{2/3} \kappa_1^{-5/3} \tag{21}$$

where $C_\kappa$ is the Kolmogorov constant, taken as $C_\kappa=1.7$ in the present study. With the available 1-D spectra, one may estimate

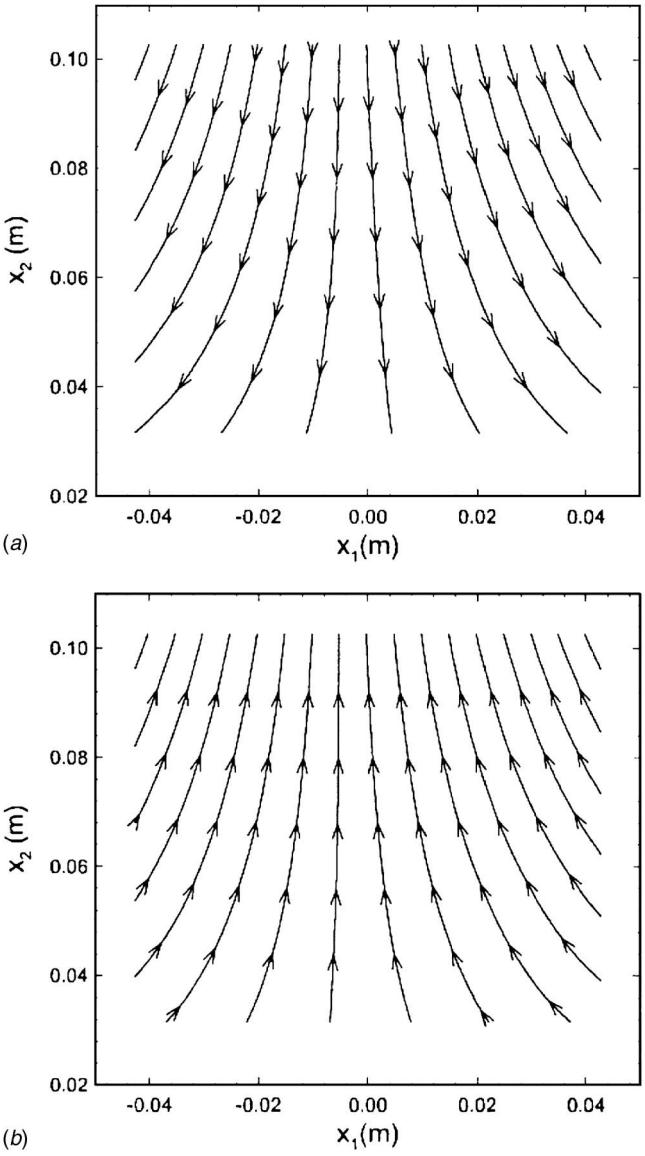


**Fig. 4 Mean flow streamline patterns at (*a*) $t=1.160$ s and (*b*) $t=2.160$ s**

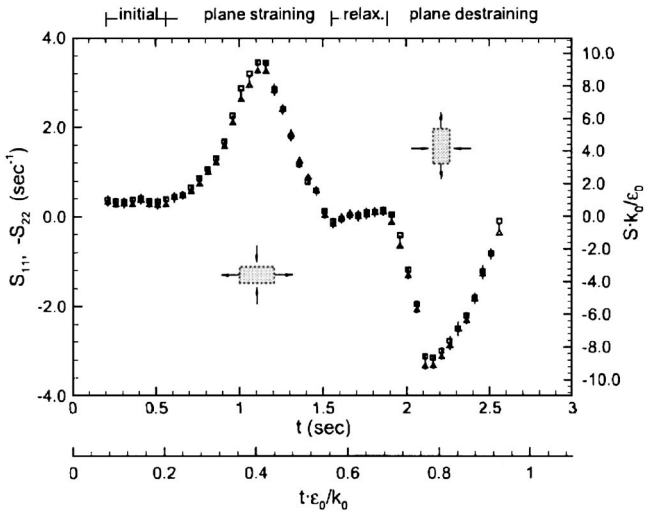


**Fig. 5 Evolution of mean strain, spatially averaged rate $S_{11}$ (squares) and $-S_{22}$ (triangles). The error bars represent the standard deviation of spatial distribution of $S(t)$.**

the dissipation rate by curve-fitting a $-\frac{5}{3}$ slope line to the data. The estimated initial dissipation rate for the present result is $\varepsilon_0 \sim 0.0035\ \mathrm{m}^2/\mathrm{s}^3$.

Other turbulence parameters of the initial equilibrium turbulence may be estimated based on $\varepsilon_0$ and characteristic turbulence rms velocity $u \equiv (u_1^{rms}+u_2^{rms})/2 \sim 0.08$ m/s. The results are: integral scale, $l_0 \sim u^3/\varepsilon_0 = 0.13$ m; turbulent kinetic energy, $k_0 = 3/2 \cdot u^2 = 0.0096\ \mathrm{m}^2/\mathrm{s}^2$; Taylor's microscale, $\lambda_0 \sim u\sqrt{15\nu/\varepsilon_0} = 0.0052$ m; Kolmogorov length scale, $\eta_0 \sim (\nu^3/\varepsilon_0)^{1/4} \sim 130\ \mu$m; and the microscale Reynolds number, $\mathrm{Re}_\lambda \sim 400$. The turbulence-to-mean-strain time scale ratio is evaluated as $S_{\max} \cdot k_0/\varepsilon_0 \sim 9.5$.

## 5 Evolution of Mean SGS Statistics

As in Liu et al. [6], we use a two-dimensional top-hat filter with scale $\Delta$, defined as

$$G_\Delta(x_1,x_2) = \begin{cases} \dfrac{1}{\Delta^2} & \text{if } |x_1| < \dfrac{\Delta}{2} \,\&\, |x_2| < \dfrac{\Delta}{2}, \\ 0 & \text{otherwise.} \end{cases} \tag{22}$$

The filtered velocities and SGS stresses are then calculated according to Eqs. (1) and (3). Convolutions are evaluated in the physical space.

**5.1 Mean SGS Dissipation.** The evolution of mean SGS dissipation is given in Fig. 8. In the present study, which is based on 2D PIV, a 2D surrogate is evaluated using only the available two-dimensional terms:

$$\Pi_\Delta = -(\langle \tau_{11}\widetilde{S}_{11}\rangle + \langle \tau_{22}\widetilde{S}_{22}\rangle + 2\langle \tau_{12}\widetilde{S}_{12}\rangle) \tag{23}$$

The analysis is repeated at three filter scales: $\Delta = 25\eta_0$, $\Delta = 50\eta_0$, and $\Delta = 100\eta_0$. One can see that for these scales, the mean SGS dissipation is positive at all times, i.e., there is no global backscatter. During the initial stage, the SGS dissipation is nearly scale independent, as expected in the inertial range. However, during the straining and destraining periods, the SGS dissipation is strongly scale-dependent. During the relaxation regime, $1.6s \leqslant t \leqslant 1.9s$, all three curves collapse, suggesting a scale-independent behavior during unforced relaxation conditions. One striking trend is that the dissipation peak in the destraining period is significantly lower than the peak in the straining period, although the amplitudes of the straining and destraining are about the same. The ratio of peak SGS dissipation during straining and destraining is about 2:1, well beyond the range that can be caused by measurement uncertainties. The cause of this trend is related to the fact that the initial condition for the destraining differs from isotropic turbulence since the relaxation to isotropy has not fully ended. This phenomenon is studied in more detail in a separate publication [35].

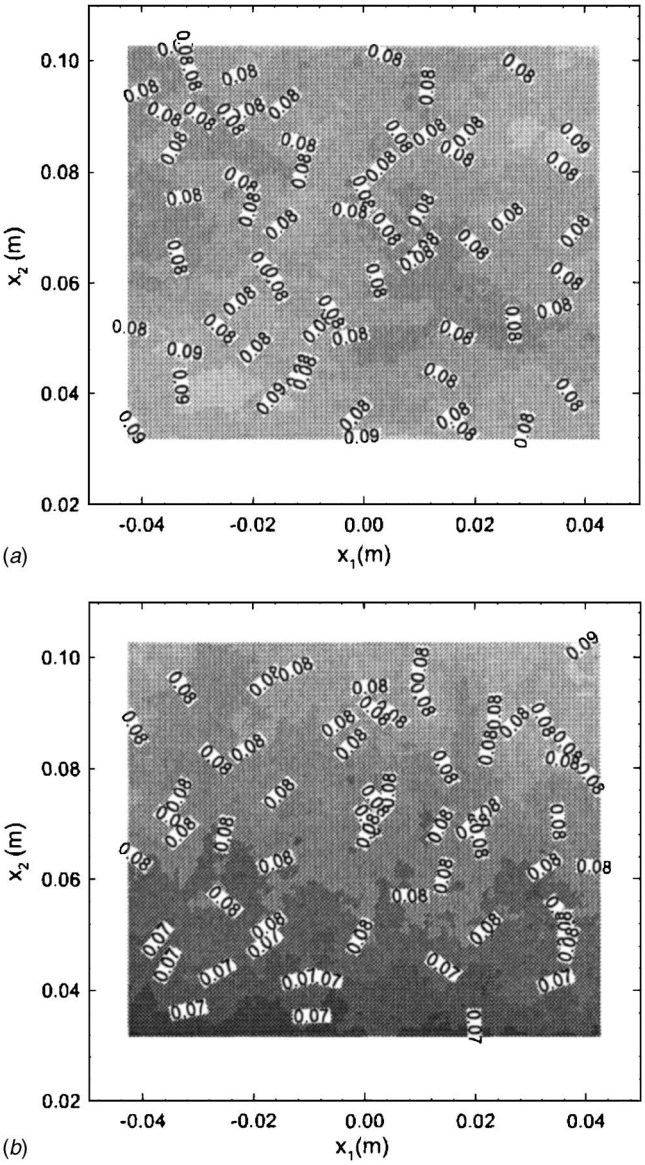


**Fig. 6 Spatial distribution of rms velocity fluctuations of the initial turbulence ($t$=0.210 s) (*a*) $u_1$ and (*b*) $u_2$**

**5.2 Dissipation Based Smagorinsky Model Coefficient.** The dissipation based Smagorinsky model coefficient at different times during the motion cycle can be computed by balancing the mean SGS dissipation and the modeled one using the Smagorinsky model, i.e.,

$$-\langle \tau_{ij}\widetilde{S}_{ij}\rangle = 2(C_S^\Delta \Delta)^2 \langle |\widetilde{S}|\widetilde{S}_{ij}\widetilde{S}_{ij}\rangle \tag{24}$$

The coefficients obtained in this way guarantee the correct reproduction of mean energetics, and thus can be used to evaluate the model coefficients determined using other approaches. The evolution of the term $2\Delta^2\langle |\widetilde{S}|\widetilde{S}_{ij}\widetilde{S}_{ij}\rangle$ at three different filter scales is presented in Fig. 9, again using a 2D surrogate evaluation based on the PIV data, which involves three terms, as in Eq. (23). The dissipation based Smagorinsky model coefficient

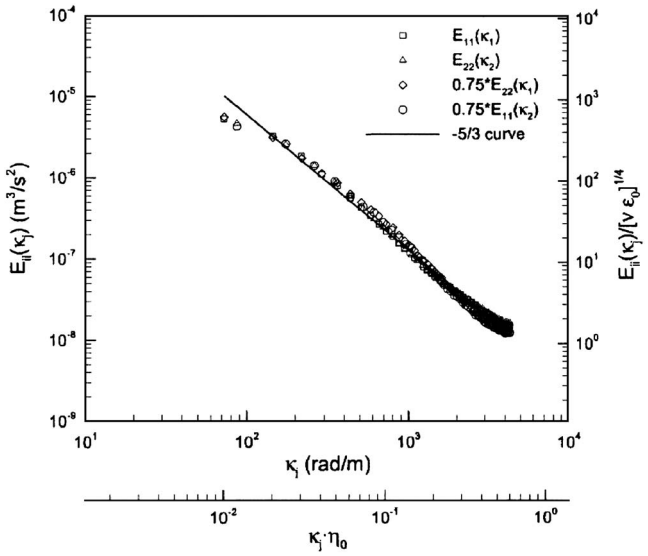


**Fig. 7 Kinetic energy spectra of the initial equilibrium turbulence ($t$=0.210 s)**

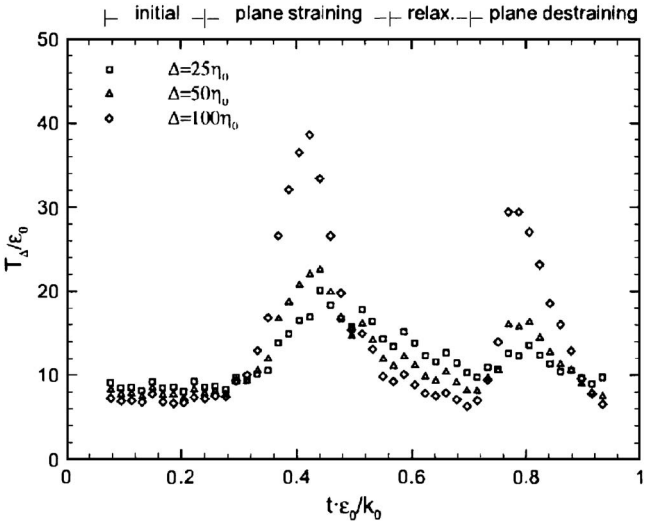


**Fig. 9 Evolution of the term $T_\Delta=2\Delta^2\langle|\tilde{S}|\tilde{S}_{ij}\tilde{S}_{ij}\rangle$ at different scales**

$$(C_S^\Delta)^2=\frac{-\langle\tau_{ij}\tilde{S}_{ij}\rangle}{2\Delta^2\langle|\tilde{S}|\tilde{S}_{ij}\tilde{S}_{ij}\rangle} \tag{25}$$

is plotted in Fig. 10 for three different filter scales. The lines in this figure (and subsequently in Figs. 11–17) represent running averages using a five-point filter with the following weights: [0:075; 0:175; 0:5; 0:175; 0:075], centered around each point. This process reduces the fluctuations in the original data, which is shown as symbols. Another line representing the static Smagorinsky model coefficient, $C_S$=0.16, is also shown. The main trends of the dissipation based coefficient during the flow evolution are as follows: after an approximately scale-invariant behavior before straining, in which $(C_S^\Delta)^2$ is in a range between 0.026 and 0.032, there is a sudden drop of $(C_S^\Delta)^2$ when the straining starts. The cause is that $2\Delta^2\langle|\tilde{S}|\tilde{S}_{ij}\tilde{S}_{ij}\rangle$ responds slightly more quickly to the applied strain than the SGS dissipation, which contains the SGS stress. After the initial decrease, the coefficients increase above the equilibrium value, with the deviation increasing with $\Delta$. The destraining period is similar, with a decrease in coefficient followed by an increase. The relaxation period is also characterized by a scale-dependent coefficient. The denominator decreases faster than the real dissipation since the former depends significantly on the applied strain, especially at large scales.

**5.3 Dynamic Smagorinsky Model Coefficient.** The Smagorinsky model coefficients determined by the standard dynamic model [Eq. (9), $\alpha$=2] at two different scales are shown in Fig. 11. For the purpose of comparison, the corresponding dissipation based Smagorinsky model coefficients at the same scale are also plotted. For $\Delta=25\eta_0$, the dynamic Smagorinsky model significantly overpredicts the coefficient during straining. Overprediction during straining is also observed at $\Delta=50\eta_0$. These results imply that the dynamic Smagorinsky model overpredicts the SGS dissipation. In fact, for $\Delta=25\eta_0$, using the static coefficient would yield more accurate results than the dynamic Smagorinsky model. For $\Delta=50\eta_0$, the dynamic Smagorinsky model overestimates the coefficient during straining by as much as the static Smagorinsky model underpredicts it.

As summarized in Sec. 1, prior work has shown that when the

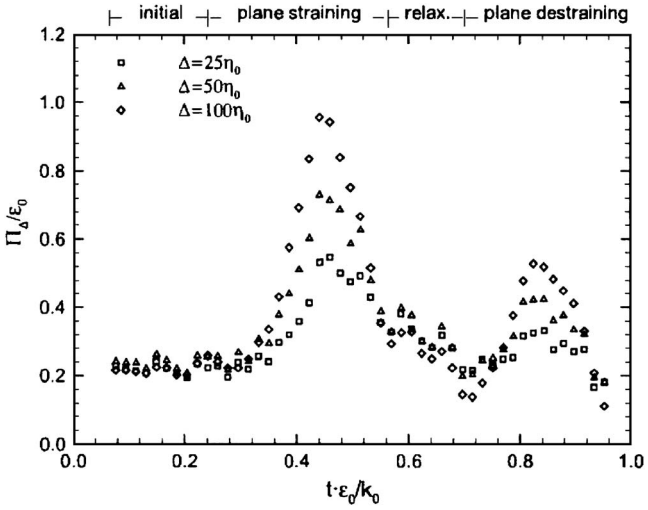


**Fig. 8 Evolution of mean SGS dissipation**

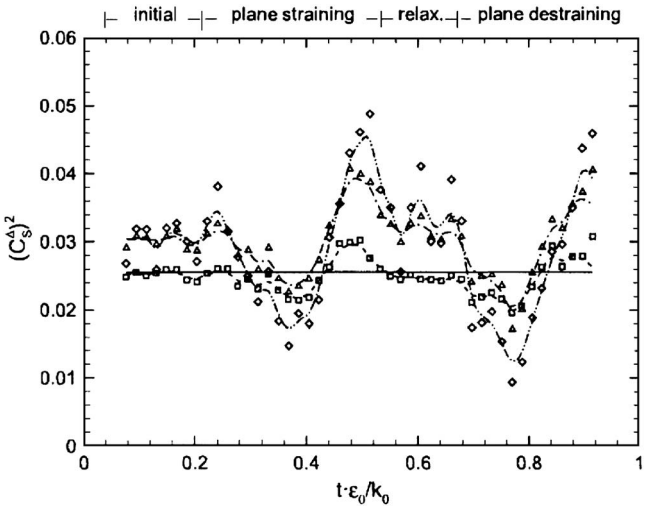


**Fig. 10 Evolution of the dissipation based Smagorinsky model coefficients $(C_S^\Delta)^2$ at three different filter scales. Squares+dash line: $\Delta=25\eta_0$, triangles+dashdot line: $\Delta=50\eta_0$, diamonds+dashdotdot line: $\Delta=100\eta_0$, and solid line: $C_S^\Delta$=0.16.**

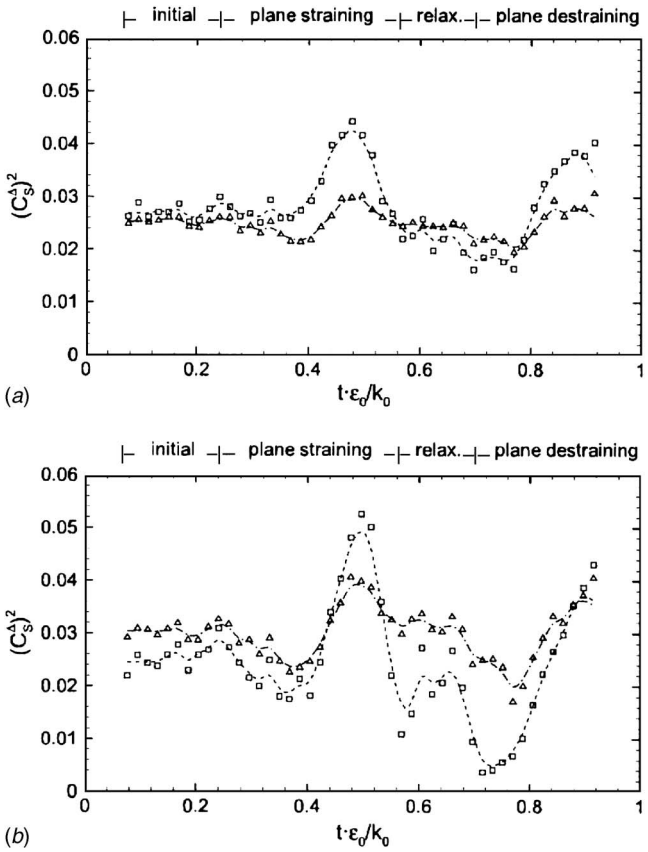


**Fig. 11 Evolution of standard dynamic model coefficients (squares and dash lines) and comparison with the dissipation based Smagorinsky model coefficients (triangles and dashdot lines, given in Fig. 12). (*a*) $\Delta=25\eta_0$ and (*b*) $\Delta=50\eta_0$.**

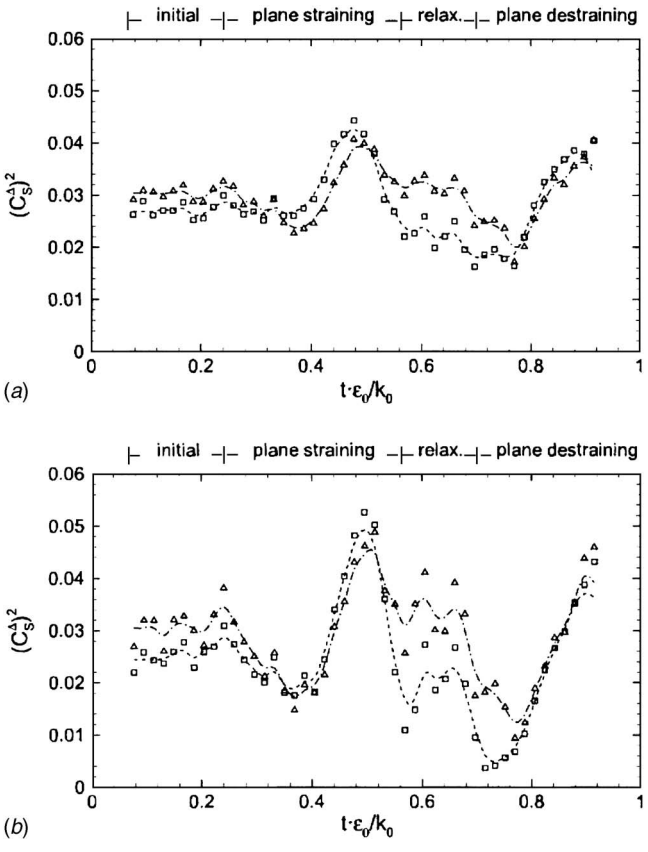


**Fig. 12 Evolution of standard dynamic model coefficient at scale $\Delta$ (squares and dash lines) compared to the evolution of the dissipation-based Smagorinsky model coefficient at scale $2\Delta$ (triangles and dashdot lines). (*a*) $\Delta=25\eta_0$ and (*b*) $\Delta=50\eta_0$.**

Smagorinsky model coefficient is scale dependent, the standard dynamic Smagorinsky model yields the coefficient appropriate for the test-filter scale ($\alpha\Delta$). To test this trend in the present data, Fig. 12 compares the Smagorinsky coefficient determined by the dynamic approach at scale $\Delta$ with the dissipation based Smagorinsky coefficient at scale $2\Delta$. As is evident, the two curves agree with each other very well during straining and destraining periods. However, the agreement does not persisit for the entire time. In particular, there are differences during the relaxation period, for both $\Delta=25\eta_0$ and $\Delta=50\eta_0$.

**5.4 Scale-Dependent Dynamic Smagorinsky Model Coefficient.** The scale-dependent dynamic Smagorinsky model requires filtering at scale $4\Delta$, and since $100\eta_0$ is the largest filter size that we can apply to our data due to its finite extent, only the $\Delta=25\eta_0$ case is amenable to analysis. Figure 13 presents the evolution of model coefficient for the scale-dependent dynamic Smagorinsky model computed according to Eq. (14). The evolutions of the dynamic and dissipation based Smagorinsky coefficients are also plotted for comparison. Right after the peak straining, i.e., between $t=1.2$ s and $t=1.4$ s the scale-dependent dynamic Smagorinsky model does give a slightly better estimation of the model coefficient than the standard (scale-invariant) dynamic Smagorinsky model, in the sense that coefficient obtained by the scale-dependent dynamic approach is lower (i.e., closer to the dissipation based coefficient) than the value obtained by the standard dynamic approach. Nevertheless, during the initial stages of straining up to the peak value, during the relaxation period, and during destraining, the prediction is worse than that of the standard dynamic Smagorinsky model. To understand the origin of this unexpected behavior, note that according to Eq. (14), the scale-dependent dynamic Smagorinsky coefficients involves the ratio of two dynamic Smagorinsky model coefficients, which are very sensitive to small phase shifts in their time response to the applied straining. To examine the phase difference, Fig. 14 compares the evolution of the two dynamic Smagorinsky coefficients, $C_S^{\Delta,DM}$ and $C_S^{2\Delta,DM}$. As is evident, during the rise of straining and destraining there is a small temporal phase mismatch between the

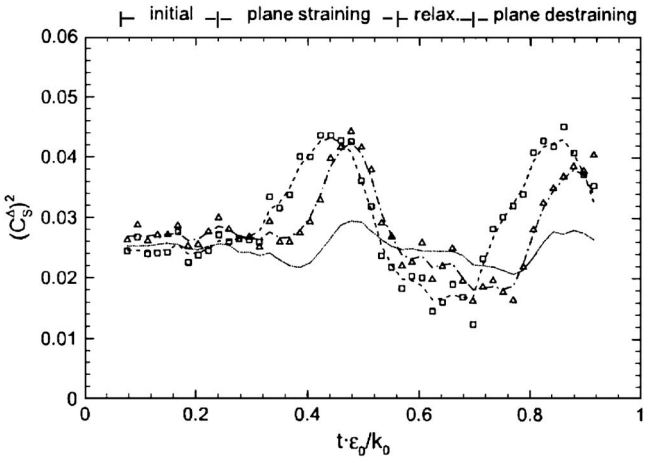


**Fig. 13 Evolution of scale-dependent dynamic model coefficient $C_S^{\Delta,SDDM}$ (squares+dash line) in comparison to the dissipation-based Smagorinsky model coefficient $C_S^\Delta$ (dotted line), and the standard dynamic model coefficient $C_S^{\Delta,DM}$ (triangles+dashdot line). $\Delta=25\eta_0$ for all three curves.**

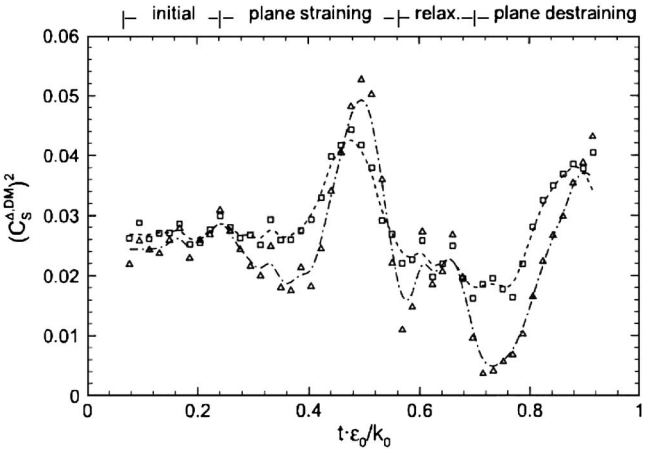


**Fig. 14 Evolution of the coefficient $C_S^{\Delta,DM}$ (squares+dash line) and $C_S^{2\Delta,DM}$ (triangles+dashdot line) for $\Delta=25\eta_0$, which are used in the scale-dependent dynamic approach, Eq. (13)**

two curves. The coefficient at the larger scale rises slightly later, and as a result it is actually smaller than the coefficient at the smaller scale, even though the coefficient at the larger scale reaches larger values later on. Such a small mismatch causes the significant overprediction of model coefficient in Fig. 13.

In summary, for $\Delta=25\eta_0$ and for this particular flow, the dynamic and scale-dependent dynamic Smagorinsky models overreact to the applied distortion, and predict coefficients that would perform worse than the static Smagorinsky model.

**5.5 Model Coefficients in Nonlinear Mixed Model.** Figure 15 shows the dissipation based model coefficient of the nonlinear mixed model, $C_{S,NL}^{\Delta}$, determined by balancing the modeled and real SGS dissipation, and by the standard dynamic approach at two scales. They show limited improvement compared to the standard dynamic Smagorinsky model results (Fig. 11). The coefficients of scale-dependent dynamic mixed model are given in Fig. 16. The scale-dependent dynamic approach again has a worse performance, which can again be attributed to a response time mismatch of the SGS stresses calculated at different filter scales.

**5.6 Uncertainty Estimates of the Measured Model Coefficients.** The uncertainty associated with the aforementioned model coefficients is difficult to evaluate formally using error propagation concepts due to the very complicated processes involving filtering, high-order moments, and differentiation, e.g., Eqs. (25), (9), and (14). Instead, we adopt a Monte Carlo approach to estimate the uncertainty and error propagation. Every vector of instantaneous measurement is contaminated by a synthetically generated noise, which follows a Gaussian distribution with zero mean and a standard deviation simulating the 0.2 pixel uncertainty of the PIV measurement. In other words, we add noise with deviation 0.0044 m/s to each velocity component. Using ten realizations of such randomly contaminated data, we observe relative differences of at most 0.3% in the computed Smagorinsky coefficients. For the standard and scale-dependent dynamic Smagorinsky models of the same test cases, the differences in the coefficients were even lower, about 0.08%.

## 6 SGS Momentum Flux

In the previous section, the effectiveness of three typical SGS models is evaluated by analyzing their ability to reproduce the correct SGS dissipation. Besides SGS dissipation, other turbulence statistics related to SGS physics are also of interest. The mean SGS stress $\langle\tau_{ij}\rangle$, or SGS momentum flux, plays a significant role in the mean momentum transport, as reflected in the ensemble average of the filtered momentum equation [Eq. (2)], when the

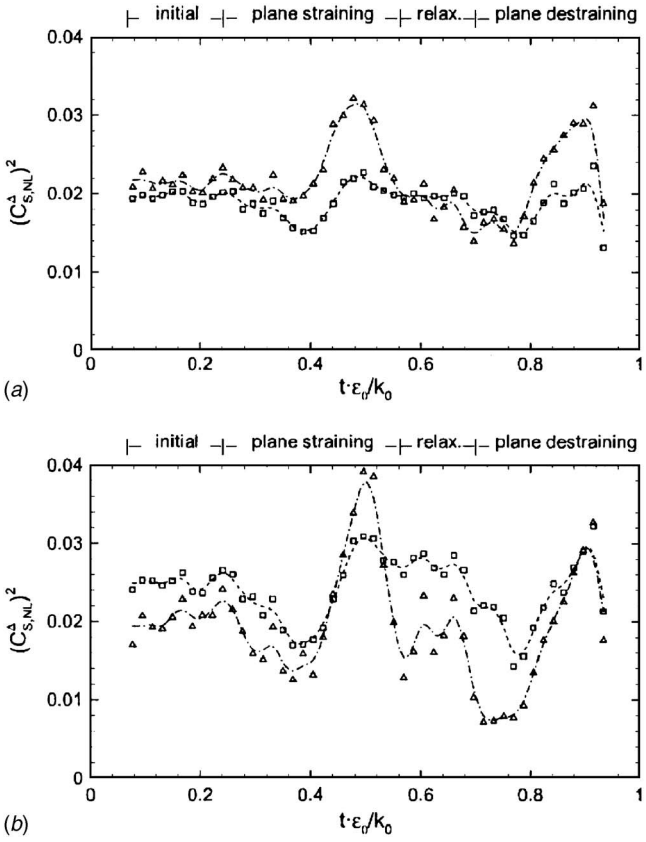


**Fig. 15 Evolution of standard dynamic coefficient $(C_{S,NL}^{\Delta,DM})^2$ of Eq. (15) (triangles and dashdot lines) in the mixed model in comparison with the dissipation-based model coefficient obtained by balancing SGS dissipation (squares and dash lines). (*a*) $\Delta=25\eta_0$ and (*b*) $\Delta=50\eta_0$.**

filter scale is not negligibly small compared to the size of the large-scale eddies. It has often been stated that the Smagorinsky models cannot reproduce both SGS dissipation and the SGS stress magnitudes simultaneously (see Refs. [1,15]). However, recently Li and Meneveau [38] have shown theoretically, from a model spectrum for strained turbulence, that as far as the mean SGS

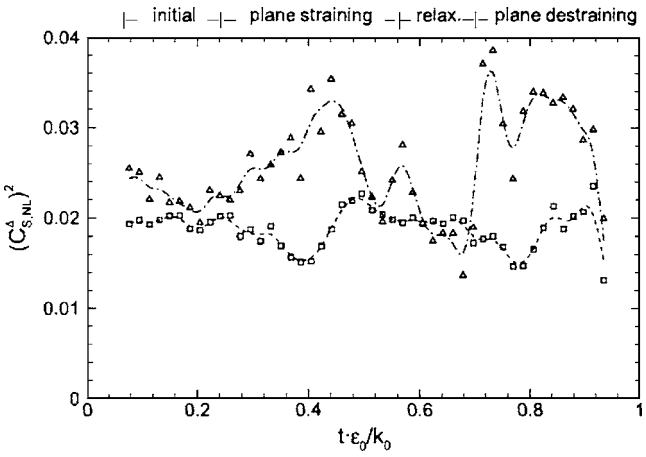


**Fig. 16 Evolution of scale-dependent dynamic nonlinear model coefficient $(C_{S,NL}^{\Delta,SDDM})^2$ of Eq. (16) (triangles and dashdot lines) in comparison with the dissipation-based nonlinear model coefficients (squares and dash lines).**

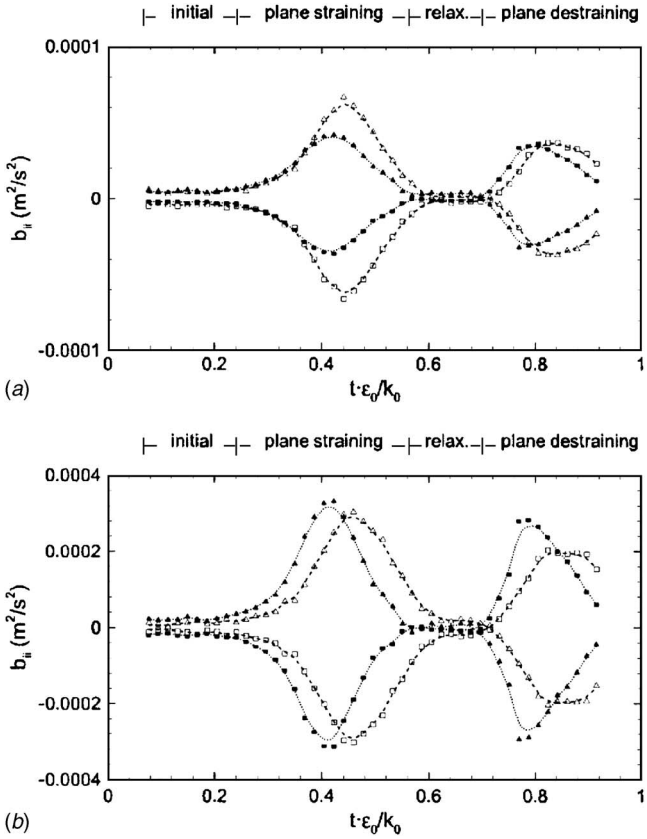


**Fig. 17 Evolution of the modeled and dissipation-based mean SGS stress anisotropy tensor terms ($b_{11}$ and $b_{22}$). (*a*) $\Delta = 25\eta_0$ and (*b*) $\Delta = 100\eta_0$. Open squares+dash lines: $b_{11}$, solid squares+dotted lines: $b_{11}^{\mathrm{mod}}$, open triangles+dash lines: $b_{22}$, and solid triangles+dotted lines: $b_{22}^{\mathrm{mod}}$.**

stress, or mean momentum flux, is concerned, the predictions from the Smagorinsky model should be fairly accurate.

We evaluate the mean SGS stress from the data. To focus upon the anisotropy, we compute a 2-D surrogate of the anisotropy tensor,

$$b_{ij} = \langle \tau_{ij} \rangle - \tfrac{1}{2} \langle \tau_{kk} \rangle \delta_{ij}. \tag{26}$$

The same quantity is computed using the static Smagorinsky model with $C_S^{\Delta} = 0.16$. The results are presented at two filter scales in Figs. 17(*a*) and 17(*b*). It is evident that the anisotropy tensor increases with $\Delta$ during straining and destraining. At both scales, during straining and destraining, the Smagorinsky model predictions are of the same order of magnitude as the real measured values, in rough agreement with the analysis of Li and Meneveau [38], which states that in the presence of weak straining $\langle \tau_{ij} \rangle \approx \langle \tau_{ij}^{\mathrm{mod}} \rangle$. In more detail, however, the Smagorinsky model underpredicts the real SGS mean stress by about 30% for $\Delta = 25\eta_0$. The result at $\Delta = 100\eta_0$ shows a different behavior. The peak is predicted well during straining and overpredicted during destraining, and the mean stress predicted by the Smagorinsky model shows a premature response compared with the real SGS momentum flux. This behavior is also consistent with the general observation that the SGS stress response is delayed with respect to the applied straining.

## 7 Conclusions

An experimental a priori study of various eddy viscosity SGS models is performed on turbulence subjected to a sequence of straining and destraining. The experiments subject initially homogeneous isotropic turbulence to 2D irrotational straining, followed by relaxation, and then by destraining. The turbulence is generated using four active grids and a computer controlled piston creating a stagnation point flow generates the straining. Planar PIV is used for measuring the velocity. The data base, consisting of 1000 vector maps at every phase of the cycle, is used for statistical analysis.

A priori tests are performed on three SGS models: Smagorinsky, standard dynamic, and scale-dependent Smagorinsky models, as well as on the nonlinear mixed models. The dissipation based Smagorinsky model coefficient is obtained by matching predicted SGS dissipation with the real one. It shows strong scale dependence during the straining-relaxation-destraining, while the turbulence is in a strong anisotropic state. The model coefficients obtained from both the standard and the scale-dependent dynamic approaches overpredict the dissipation based Smagorinsky coefficient. The model coefficient at scale $\Delta$ in the standard dynamic model is close to the dissipation based Smagorinsky coefficient at scale $2\Delta$. Still, the scale-dependent dynamic model does not yield improvements, and in some cases even worsens the predictions, due to subtle phase lags between the responses at different scales. The dynamic and scale-dependent dynamic nonlinear mixed models do not show an improvement, at least as far as evolution of the coefficients is concerned. We conclude that the mismatch between stress and strain-rate tensor responses to the applied straining causes, in the present experiment, difficulties for turbulence modeling based on a purely algebraic SGS closure.

It should be pointed out that the present measurements of coefficients and comparisons are performed by neglecting the effects of the third velocity component. Three-dimensional measurements are needed to quantify the effects of this approximation, although it appears unlikely that it could affect the observed mismatch between scales significantly.

The prediction of mean SGS momentum flux from the Smagorinsky model is correct in terms of order of magnitude, which is surprising, but in agreement with a recent theoretical result of Li and Meneveau [24]. However, the delayed response of the SGS stress compared to the strain rate also affects the agreement of mean stresses. The present results provide support for an approach of involving a solution to additional transport equation for the SGS kinetic energy, although such an approach requires specification of three model parameters (see Ref. [39]).

## Acknowledgments

The authors would like to thank research engineers Y. Ronzhes for his close involvement in facility design, and S. King for his assistance in system integration. This research is sponsored by the Office of Naval Research, under Grant No. N0014-03-0361, monitored by program officer Dr. Ronald Joslin.

## References

[1] Pope, S., 2000, *Turbulent Flows*, Cambridge University Press, Cambridge.
[2] Townsend, A., 1954, "The Uniform Distortion of Homogeneous Turbulence," Q. J. Mech. Appl. Math., **7**(1), pp. 104–127.
[3] Keffer, J., 1965, "The Uniform Distortion of a Turbulent Wake," J. Fluid Mech., **22**, pp. 135–160.
[4] Tucker, H., and Reynolds, A., 1968, "The Distortion of Turbulence by Irrotational Plane Strain," J. Fluid Mech., **32**, pp. 657–673.
[5] Lee, M., and Reynolds, W., 1985, *Numerical Experiments on the Structure of Homogenous Turbulence*, Stanford University Report, TF-24
[6] Liu, S., Katz, J., and Meneveau, C., 1999, "Evolution and Modeling of Subgrid Scales During Rapid Straining of Turbulence," J. Fluid Mech., **387**, pp. 281–320.
[7] Germano, M., Piomeeli, U., et al., 1991, "A Dynamic Subgrid-Scale Eddy Viscosity Model," Physica A, **3**, pp. 1760–1765.
[8] Rogallo, R., and Moin, P., 1984, "Numerical Simulation of Turbulent Flows," Annu. Rev. Fluid Mech., **16**, p. 99.
[9] Reynolds, W., 1990, "The Potential and Limitation of Direct and Large Eddy Simulations," in *Whither Turbulence? Or Turbulence at Crossroads*, edited by J. L. Lumley, Springer, New York.
[10] Piomelli, U., Cabot, W. H., Moin, P., and Lee, S., 1991, "Subgrid-Scale Backscatter in Turbulent and Transitional Flows," Phys. Fluids A, **3**(7), pp. 1766–1771.

[11] Liu, S., Meneveau, C., and Katz, J., 1994, "On the Properties of Similarity Subgrid-Scale Models as Deduced From Measurement in Turbulent Jet," J. Fluid Mech., **275**, pp. 83–119.
[12] Lesieur, M., and Metais, O., 1996, "New Trends in Large-Eddy Simulations of Turbulence," Annu. Rev. Fluid Mech., **28**, pp. 45–82.
[13] Smagorinsky, J., 1963, "General Circulation Experiments With the Primitive Equations, Part 1: The Basic Experiment," Mon. Weather Rev., **91**, pp. 99–164.
[14] Leonard, A., 1997, "Large-Eddy Simulation of Chaotic Convection and Beyound," AIAA Pap. 97-0204.
[15] Meneveau, C., and Katz, J., 2000, "Scale-Invariance and Turbulence Models for Large-Eddy Simulation," Annu. Rev. Fluid Mech., **32**, pp. 1–32.
[16] Borue, V., and Orszag, S. A., 1998, "Local Energy Flux and Subgrid-Scale Statistics in Three Dimensional Turbulence," J. Fluid Mech., **366**, pp. 1–31.
[17] Piomelli, U., Moin, P., and Ferziger, J., 1988, "Model Consistency in Large Eddy Simulation of Turbulent Channel Flows," Phys. Fluids, **31**(7), pp. 1884–1891.
[18] Meneveau, C., 1994, "Statistics of Turbulence Subgrid-Scale Stresses: Necessary Conditions and Experimental Tests," Phys. Fluids, **6**(2), pp. 815–833.
[19] O'Neil, J., and Meneveau, C., 1997, "Subgrid-Scale Stresses and Their Modelling in a Turbulent Plane Wake," J. Fluid Mech., **349**, pp. 253–293.
[20] Tao, B., Katz, J., and Meneveau, C., 2002, "Statistical Geometry of Subgrid-Scale Stresses Determined From Holographic Particle Image Velocimetry Measurements," J. Fluid Mech., **467**, pp. 35–78.
[21] Porte-Agel, F., Parlange, M. B., Meneveau, C., and Eichinger, W. E., 2001, "A Priori Field Study of the Subgrid-Scale Heat Fluxes and Dissipation in the Atmospheric Surface Layer," J. Atmos. Sci., **58**, pp. 2673–2698.
[22] Kleissl, J., Meneveau, C., and Parlange, M., 2003, "On the Magnitude and Variability of Subgrid-Scale Eddy-Diffusion Coefficients in the Atmospheric Surface Layer," J. Atmos. Sci., **60**, pp. 2372–2388.
[23] Lilly, D. K., 1967, "The Representation of Small-Scale Turbulence in Numerical Simulation Experiments," in Proc. IBM Scientific Computing Symp. Environ. Sci., p. 195.
[24] Lilly, D. K., 1992, "A Proposed Modification of the Germano Subgrid-Scale Closure Method," Phys. Fluids A, **4**, pp. 633–635.
[25] Meneveau, C., and Lund, T. S., 1997, "The Dynamic Model and Scale-Dependent Coefficient in the Viscous Range of Turbulence," Phys. Fluids, **9**, pp. 3932–3934.
[26] Porte-Agel, F., Meneveau, C., and Parlange, M., 2000, "A Scale-Dependent Dynamic Model for Large-Eddy Simulation: Application to a Neutral Atmospheric Boundary Layer," J. Fluid Mech., **415**, pp. 261–284.
[27] Bou-Zeid, E., Meneveau, C., and Parlange, M., 2005, "A Scale-Dependent Lagrangian Dynamic Model for Large Eddy Simulation of Complex Turbulent Flow," Phys. Fluids, **17**, p. 025105.
[28] Meneveau, C., Lund, T., and Cabot, W., 1996, "A Lagrangian Dynamic Subgrid-Scale Model of Turbulence," J. Fluid Mech., **319**, pp. 353–385.
[29] Makita, H., 1991, "Realization of a Large-Scale Turbulence Field in a Small Wind Tunnel," Fluid Dyn. Res., **8**, pp. 53–64.
[30] Mydlarsky, L., and Warhaft, Z., 1996, "On the Onset of High-Reynolds-Number Grid-Generated Wind Tunnel Turbulence," J. Fluid Mech., **320**, pp. 331–368.
[31] Roth, G., Mascenik, D., and Katz, J., 1999, "Measurement of the Flow Structure and Turbulence Within a Ship Bow Wave," Phys. Fluids, **11**, pp. 3512–3523.
[32] Roth, G., and Katz, J., 2001, "Five Techniques for Increasing the Speed and Accuracy of PIV Interrogation," Meas. Sci. Technol., **12**, pp. 238–245.
[33] Keane, R., and Adrian, R., 1990, "Optimization of Particle Image Velocimeters, Part I, Double Pulsed Systems," Meas. Sci. Technol., **1**, pp. 1202–1215.
[34] Huang, H., Dabiri, D., and Gharib, M., 1997, "On Errors of Digital Particle Image Velocimetry," Meas. Sci. Technol., **8**, pp. 1427–1440.
[35] Chen, J., Meneveau, C., and Katz, J., 2005, "Scale Interactions of Turbulence Subjected to a Straining-Relaxation-Destraining Cycle," J. Fluid Mech., submitted.
[36] Nimmo-Smith, W., Katz, J., and Osborn, T., 2005, "Flow Structure in the Bottom Boundary Layer of the Coastal Ocean," J. Phys. Oceanogr., **35**(1), pp. 72–93.
[37] Monin, A., and Yaglom, A., 1971, *Statistical Fluid Mechanics*, MIT Press, Cambridge.
[38] Li, Y., and Meneveau, C., 2004, "Analysis of Mean Momentum Flux in Subgrid Models of Turbulence," Phys. Fluids, **16**, pp. 3483–3486.
[39] Wong, V. C., 1992, "A Proposed Statistical-Dynamic Closure Method for the Linear or Nonlinear Subgrid-Scale Stresses," Phys. Fluids, pp. 1080–1082.